The final publication is available at

https://doi.org/10.1177/1468087420972544

Additional Information

Assessment of the numerical and experimental methodology to predict EGR cylinder-to-cylinder dispersion and pollutant emissions

J. Galindo[a], H. Climent[a], R. Navarro[a], G. García - Olivas[a,*]

[a]CMT - Motores Térmicos, Universitat Politècnica de València
Camino de Vera, 46022 Valencia (Spain)

Abstract

EGR cylinder-to-cylinder dispersion poses an important issue for piston engines, since it increases NOx and particulate matter (PM) emissions. In this work, the EGR distribution on a 6-cylinder intake manifold is analyzed by means of experiments, 0D/1D engine modeling and 3D CFD simulations at 3 different working points. Using a comprehensive set of measurements, statistical regressions for NOx and PM emissions are developed and employed to quantify the sensitivity of numerical configuration to EGR dispersion and subsequent increase of pollutants. CFD mesh and time-step size independence studies are conducted, taking into account their interrelation through the Courant number. The obtained numerical configuration is validated against experimental measurements, considering different unsteady RANS turbulence submodels ($k - \varepsilon$ and $k - \omega$) as well as the inviscid case. The agreement of the different approaches is quite sensitive to the operating conditions, obtaining root mean square errors for the average cylinder-to-cylinder EGR distribution between $1 - 17\%$ and for the transient CO_2 traces between $8 - 29\%$. However, for the worst-case scenario, the error in NOx and PM emissions prediction is below 2%. The regressions are employed to justify the increase of EGR distribution impact on pollutants when EGR rate or dispersion is increased. Flow investigation reveals the underlying reasons for the discrepancies and similarities between the predictions of the different turbulence submodels.

Keywords: EGR distribution, CFD setup, Flow mixing, Engine model, NOx-Particulate Matter regression analysis, Intake manifold

1. Introduction and literature review

In recent decades, the effects of pollutant emissions in terms of health issues, climatic change and global warming have been demonstrated. Therefore, the emission standards have become more and more restrictive regarding the Internal Combustion Engines (ICEs) to get a reduction in the pollutants. Due to these standards, several techniques have been developed to reduce emissions while trying to keep the performance of the engine. Regarding these techniques, the Exhaust Gas Recirculation (EGR) has become one of the most developed emission

control procedure [1, 2]. In this technique, a controlled fraction of the exhaust gases is reintroduced in the intake line, with the aim of reducing the maximum temperature in the combustion chamber, due to the dilution of the fresh air and absorption of a part of the heat released during combustion [2]. With this reduction of temperature, the formation of Nitrogen Oxides (NOx) are consequently decreased with little penalty in increased particulate emissions, as long as the EGR rates are below a certain threshold [1].

In turbocharged engines, the EGR can be implemented using one of the following two configurations. If the exhaust gases are taken upstream the turbine and reintroduced in the intake line downstream the compressor, the method is called high

---
*Corresponding author. Tel.: +34 963 877 650
Email addresses: `galindo@mot.upv.es` (J. Galindo),
`hcliment@mot.upv.es` (H. Climent), `ronagar1@mot.upv.es` (R. Navarro), `guigarol@mot.upv.es` (G. García - Olivas)

pressure EGR (HP-EGR). When the exhaust gases are extracted downstream the turbine and reintroduced before the compressor, it is known as low pressure EGR (LP-EGR) configuration. A heat exchanger can be used in both configurations to reduce the exhaust gas temperature just before its reintroduction in the intake line. In fact, Desantes et al. [2] demonstrates that both configurations can be combined, and different control methods have been developed to taking the optimal configuration depending of the operating point [3]. These control methods have been developed because both techniques have advantages and drawbacks. Regarding LP-EGR configuration, it takes exhaust gases downstream the after-treatment devices, so the problems of soot deposition in the EGR line are avoided. Nevertheless, an important issue in this configuration is the condensation that can appear before the compressor in cold operating conditions [4, 5, 6], that compromises the compressor integrity [7]. The HP-EGR configuration is still the most employed in ICEs due to its simplicity, the faster engine response [8] and the reduction in the pumping losses [2]. The challenge of this approach is achieving a homogeneous distribution of the exhaust gases in all the cylinders of the engine [9]. If the EGR distribution between the cylinders is very different, the amount of NOx and particulate matter (PM) will increase, as was demonstrated by Maiboom et al. [10]. Therefore, the mixing before the cylinders in the HP-EGR technique is essential to avoid this increase of the emissions.

The behavior of the mixing between the air and the EGR streams can be studied by experimental techniques as well as numerical simulations. In the experimental measurements, the real behavior of the flow can be assesses through average and instantaneous values [9, 11]. The experimental approach main drawbacks include the necessity (and) of manufacturing the real parts involved and installing them in an engine test cell, the difficulty of instrumenting and performing non-invasive measurements in some engine locations and even the impossibility of providing a time-resolved measure of some relevant variables. To overcome these issues, a convenient choice is to conduct nu-

merical simulations combining 0D/1D engine models and 3D Computational Fluid Dynamics (CFD). Obviously, these models need to be validated with the corresponding experimental measurements to guarantee the required accuracy.

In this work, EGR cylinder-to-cylinder dispersion will be predicted at different operating conditions. A calibrated 0D-1D engine model will provide boundary conditions for 3D CFD simulations of the intake manifold. The commercial CFD code STARCCM+ v.12.06 [12] will be used throughout all the study. The numerical predictions will be compared with equivalent experimental simulations. The impact of including the 3D CFD model on the results will be assessed. The influence and interrelation between CFD mesh and time-step size on EGR distribution will be analyzed as well. Moreover, turbulence modeling will be evaluated in terms of EGR dispersion as well as CO_2 transient traces and flow field prediction.

Besides, the influence of the obtained EGR dispersion on pollutant emissions will be assessed by means of NOx and PM models [13, 14]. Usually these models are applied to experimental measurements [15] or embedded into 0D-1D engine models. In this work, they will be applied to CFD results in order to quantify the impact of the numerical configuration in the predictions of contaminant. With this, the sensitivity and trade-off of the CFD setup in terms of accuracy will be properly assessed.

In section 2, the experimental methods, the engine 0D/1D model and the manifold 3D CFD model will be described. The sensitivity of 3D CFD simulations to the mesh refinement, time-step size and choice of turbulence model will be discussed in section 3. With the selected final setup, the average and instantaneous validation of different turbulence modeling approaches will be performed in different operating points in section 4. Section 5 is devoted to provide some guidelines of the behavior of the flow in these operating points. Finally, the main conclusions of this document will be exposed in section 6.
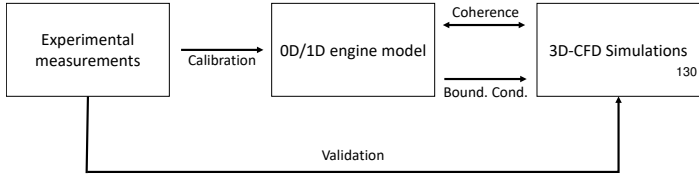
2

Figure 1: Flow chart of methodology employed to predict EGR dispersion.

2. Methods

The methodology followed in this work in order to predict EGR cylinder-to-cylinder distribution is depicted in Figure 1. The experimental measurements described in section 2.1 will be useful to calibrate the engine simulation software as well as to conduct a regression analysis between the EGR rate of the engine and its NOx and PM emissions. The 3D CFD model of the intake manifold is set with the baseline configuration commented in section 2.2. The calibrated 0D/1D engine model (section 2.3) will provide instantaneous mass flow rates and temperatures that will be applied as boundary condition for the 3D-CFD simulation. The consistency between the 1D and 3D modeling of the intake manifold will be assessed. Finally, the results provided by the 3D CFD simulations will be validated against the experimental measurements in terms of average and instantaneous results.

2.1. Experimental apparatus

2.1.1. Experimental measurements

This section is devoted to expose the main elements of the experimental facility and the conducted measurements used to calibrate the 0D/1D engine model and for the validation of the 3D models. The turbodiesel engine analyzed in these experiments presents a displacement of 8 liters with 6 cylinders and 24 valves, with a HP-EGR system coupled to reduce pollutant emissions and approved by the *Euro VI Heavy-Duty* standard. The main features of the experimental facility are very similar to the exposed in the works of Luján et al. [3, 11].

To achieve a good calibration of the engine simulation software that will be employed in this document, more than 10 operating points have been measured in different regions of the engine map. In addition, in every operating point, different EGR rates have been applied to obtain the impact on pollutant emissions getting useful data to adjust the HP-EGR configuration. From these essays, both average and instantaneous values have been measured. In several zones of the intake manifold that will be indicated in section 2.2.1, and upstream the aftertreatment devices, mean CO_2 has been measured with *Horiba Mexa 7100DEGR* probes. By these probes, CO_2 and temperature are obtained when the signal is stable. Taking into account that the CO_2 exhaust percentage is known, the EGR rate can be obtained according to Luján et al. [9] (see Appendix A.1). The NOx level in parts per millions (ppm) and the particulate matter in FSN (filter smoke number) are measured upstream the aftertreatment devices, in order to obtain the main emission indicators in every operating point. The 0D/1D model needs pressure traces to be calibrated in a proper way, so instantaneous pressure probes have been placed at the inlet of air and EGR ducts, upstream of the numerical domain. In addition, the instantaneous percentage of CO_2 along an engine cycle is provided by the fast measurements probes of CO_2 (*Cambustion©* device). These experimental sensors are located in holes previously prepared taking into account the geometrical constraints of the manifold.

2.1.2. NOx-PM statistical regression

As commented in section 1, high EGR dispersion between cylinders can produce a huge increment in the PM or NOx emission depending of the excess or lack of EGR rate, respectively. A statistical regression based feeded with experimental measurements has been employed in this work to translate the EGR distributions of the 3D-CFD models into emission indicators. With this, the sensitivity and trade-off between 3D model accuracy and computational effort can be properly addressed in section 3.

Different models have been proposed to predict pollutant emissions in accordance with the EGR rate imposed to the engine in every operating point. In the present work, the model

developed by Guardiola et al. [13] has been applied. In this model, NOx emissions are normalized with the emission in 0% EGR rate case ($NO_x/NO_{x,EGR=0}$). Regarding the particulate matter (PM), since emissions with no EGR are near 0, it is not necessary to normalize with this rate, and will be represented with the filter smoke number (FSN) indicator. Guardiola et al. [13] demonstrated that the factor $EGR \cdot 1/\lambda$, being λ the excess of air, is the most appropriated to make a coherent statistical regression and will be the independent variable for this fitting. The regression regarding NOx is adjusted with an exponential function, in the same way than the works of Guardiola et al. [13]. On the other hand, particulate model is adjusted with a 3rd degree polynomial function. In this way, both regressions are applied to the experimental measurements described in section 2.1.1, getting the graphs presented in Figure 2

In Figure 2, both regressions for NOx emissions and PM are depicted. It must be noticed that the PM model is normalized too with the maximum value. It is clear in this case that the particulate matter grows up in a huge way starting at a certain threshold, while the NOx emissions are reduced in a asymptotic way when the EGR rate are increased. Taking into account that the correlation coefficients (R^2) are beyond the 90%, in the same order than the agreement coefficient of Guardiola et al. [13], both fittings can be applied to each and every cylinder of the 3D-CFD models, to predict the impact of the EGR dispersion in emissions.

The concave shape of the NOx and FSN (PM) curves (see Figure 2) illustrate the issue with EGR dispersion. When 2 cylinders depart from the nominal EGR (one swallowing more EGR than it should and the other one less, to keep the EGR balance), the increase of emissions in one cylinder (lack of EGR for NOx and EGR excess for PM) is greater than the decrease of contaminants existing in the other cylinder, so the overall emissions are higher than with a uniform EGR distribution. This non-linear behavior is more noticeable depending on the value of $EGR \cdot 1/\lambda$ of the working point.

Figure 2: Correlation with experimental data using exponential function in the NOx emissions (top) and polynomial function in the PM emission (bottom).

2.2. 3D CFD baseline setup

2.2.1. Geometry

The 3D CFD numerical domain, corresponding to the 6 cylinder intake manifold of the engine described in section 2.1.1, is presented in Figure 3.

Figure 3 shows on one side the global perspective of the manifold, and a detailed view of the valves in the intake and EGR lines. The EGR inlet boundary is placed several diameters upstream the EGR valve, while the fresh air inlet is placed upstream the throttle valve. The geometry of this 6 cylinder manifold is different to the ones described in other works like [16, 17] and is more similar to the manifolds in which the 2 streams of air and EGR are mixed in a T-Junction, like the manifolds that appear in [9, 18] and specially to the geometry studied

Figure 3: 3D computational domain with air inlet boundary (blue), EGR inlet boundary (red) and outlets boundaries (orange) (top figure) and detailed view of EGR valve (bottom left) and throttle valve (bottom right), indicating their corresponding degree of freedom.
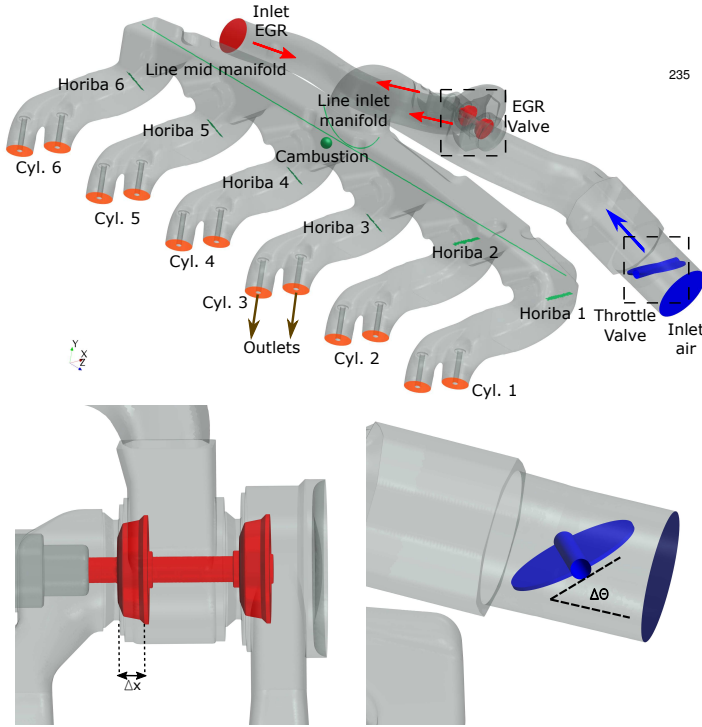
in the works of Sakowitz et al. [19]. Nevertheless, the impact of different mixer geometries in the EGR distribution is out of the scope of this work.

Bottom left side of Figure 3 provides a close-up of the EGR double-seat valve, which connects the EGR line with 2 ducts that will meet the fresh air pipe so as to produce the EGR-air mixing. Notice that the EGR valve has an axial displacement to regulate the EGR rate, so this displacement depends on the operating point of the engine. In the same way, the throttle valve opening (bottom right side of Figure 3) can be regulated. Both valves are adjusted with the same displacement or angle than in the experimental measurements, in accordance with Table 1. In Figure 3, the postprocessing probes are highlighted in green color. The *Horiba Mexa 7100DEGR* probes are modeled as a tiny surface, representing the area aspirated by the real probes. Appendix A.1 shows the method to estimate the EGR rate on the basis of the EGR mass fraction gathered by the

Horiba virtual probes. Notice that, due to the heterogeneity of the flow, the EGR rate obtained with this probes may not be the same than the EGR that the cylinders will swallow, which is the relevant EGR rate but cannot be measured. Therefore, an estimation of these deviations is obtained in Appendix A.2. The Cambustion© probe is modeled as a point in the same place than the real one, to provide the instantaneous EGR rate that will be used in the validation of the 3D models.

2.2.2. Turbulence model

Turbulence modeling is one of the most important issues to be taken into account in an EGR dispersion problem as mentioned in section 1, due to the relevance of the mixing process between air and EGR streams in some geometries or operating points of the engine. Regarding the LES approach, its ability to solve a significant fraction of the turbulent scales should allow an accurate prediction of mixing problems, ranging from simple geometries as T-junction [20, 21] to EGR dispersion in intake manifold s ([19, 20, 22, 23]). RANS approach has been used as well in this type of problems [24, 25]. Therefore, the decision of modeling turbulence in a more detailed way as LES o more simplified as RANS needs to be addressed. Sakowitz et al. [20] demonstrate that the turbulence structures in a T-junction are not been captured properly with the RANS approach, being too diffusive and with little mixing capacity. In spite of this fact, a different work by Sakowitz et al. [19] show how the air-EGR mixing in the intake manifold at low frequencies (∼ 60 Hz), RANS approach and LES approach produce similar results, likely because the EGR dispersion in these conditions is more governed by the EGR pulses rather than the turbulence mixing. This behavior will be studied in sections 4 and 5.

In the numerical domain presented in Figure 3 the influence of the pulsating effects can be remarkable due to the low frequencies in the considered operating points. Therefore, the URANS approach (*unsteady RANS*) can be a suitable option to get a trade-off between accuracy of the results and computational effort. Particularly, the literature shows a variety of

works providing a good agreement between CFD 3D predictions with URANS approach, employing a $k - \varepsilon$ closure model [16, 24, 25, 26]. Thereby, the URANS approach with the $k - \varepsilon$ turbulence submodel has been selected to be the baseline setup of this work. In most of these cited works, the turbulence model is fixed throughout the study. On the contrary, in this work, the influence of the turbulence submodels in EGR dispersion will be assessed, including simulations with $SST\ k - \omega$ turbulence submodel in section 4. In addition, the possibility of neglecting the impact of turbulence is considered by employing the inviscid model as well.

2.2.3. Rest of CFD configuration

The remaining features of the baseline CFD setup are summarized as follows:

- A polyhedral mesh has been employed, improving the resolution of the flow close to the walls by means of a prism layer. The baseline mesh uses 6M cells, but a grid indepencence analysis is conducted in section 3, in which more details about the mesh are provided.

- The air and EGR have been modeled as different non-reactive gas component, instead of EGR being modeled as passive scalar like other works [19]. The main thermodynamical properties of the EGR are variable with temperature.

- The segregated solver has been used for the resolution of the numerical equations. A coupled solver would be more adequate to solve cases with high Mach numbers. For the considered operating points, the highest values of Mach are far from transonic values (maximum instantaneous local Mach number below 0.5), so the selected segregated solver is a suitable approach.

- The temporal scheme of the simulations is implicit. Initial time step of the setup is 2°/step in terms of engine crankshaft revolutions, in the same order that the steps in the work of Dimitriou et al. [24]. Subsequently, in sec-

tion 3, a sensitivity study of time-step size will be carried out.

- Another important issue to consider is the convergence criteria of the analyzed cases. Since all the cases are unsteady and pulsating, the variables should be cycle-averaged after reaching periodicity. The number of engine cycles to average the results are variable depending of the works and the considered operating points. For example, in the works of Sakowitz et al. [19, 23, 27], the number of cycles vary between 4-10-20 cycles in LES calculations. On the other hand, in 3D RANS coupled with engine simulation software, the number of cycles calculated previously to the coupling are about 10-15 cycles [17, 24]. Taking into account the achieved results, the number of cycles to make a proper average in this work are about 7-11, depending of the considered operating point.

    - After several studies in the under-relaxation factors, the inner iterations to provide convergence at each time step have been fixed in 10.

- The influence of the boundary condition type was assessed by Galindo et al. [28]. According to these studies, imposing $\dot{m}_{inlet} - \dot{m}_{outlet}$ as boundary conditions showed better numerical behavior and get reasonable agreement with experimental measurements than other types, so the same approach is employed in this work. A 0D/1D engine model is developed in section 2.3 so as to provide the transient traces of these mass flow rates, to be used as boundary conditions by the 3D CFD model.

2.3. 0D/1D engine model

As mentioned in section 2.1, the experimental data allows to obtain the main variables used to calibrate and modify the 0D/1D model of the engine. At the same time, this engine model will be the method to obtain the main boundary conditions of the 3D CFD model (see Figure 1), in the fashion of

6

other works [29, 22].

The 0D/1D model has been developed in *GT-Power* software, which allows to get a prediction of relevant variables at all engine locations, as long as the model is properly calibrated. The main objective in the calibration is to tune the model coefficients (pressure loss and heat transfer coefficients) in order to match the engine measurements at the corresponding operating point. In this way, the accuracy of the prediction of the required variables to be used as boundary conditions for the 3D CFD model is guaranteed. When an engine simulation is performed, the model has to reach a steady state, in the way that the main variables are periodic. In the present work, the engine model requires the determination of the VGT angle, which controls the intake pressure and is known from the corresponding experimental, and the EGR valve position (Figure 3), which sets the EGR rate in the essays. More details about the calibration of the engine model can be found in the work of Galindo et al. [28].

In EGR dispersion problems, Galindo et al. [30] discuss the possibility of performing 1D-3D co-simulations by coupling the engine model with the 3D CFD model of the intake manifold, to get a perfect agreement in the boundary conditions of the domain [17, 24]. However, this type of "strong" coupling entails an increase of computational effort, together with other constraints [30]. In this work, the calibrated engine simulation results have been imposed to the 3D models as boundary conditions only in a 1-way direction [29]. Since this approach may produce inconsistencies between the 1D and 3D modeling of the intake manifold, a feedback loop is conducted as a sort of 'weak' coupling [30] to guarantee the coherence between both representation of the manifold (see Figure 1). In this way, in some operating points the 0D/1D model has been calibrated again to match the 3D CFD results in terms of overall mass flow rate and pressure pulses. This feedback loop is repeated until the differences in such variables are lower than 5% in average values and 10% in peak-to-peak amplitude. Once the weak coupling is finished, the mass flow rate traces predicted by the

0D/1D model are updated to provide new boundary conditions for the 3D CFD model.

2.4. Operating points

In this work, EGR dispersion is predicted at 3 different engine working points. These operating points cover low, medium and high power range of the engine, being summarized in Table 1. In section 3, the sensitivity studies will be calculated with operating point 2, because it is a representative working condition located in the middle of the engine map, with similar speed and load conditions as the points used by Sakowitz et al. [19, 27]. On the other hand, point 1 has been tested to check EGR distribution at low load and low rpm, with throttle and EGR valve regulated to provide the greatest EGR rate studied in this work. Operating point 3 is tested at high loads and lower EGR rate with the throttle valve fully open.

Table 1: Operating Points

Operating point	1	2	3
Engine speed	Low	Medium	High
BMEP	Low	Medium	High
EGR rate (%)	20	15	10
$EGR \cdot 1/\lambda$	7	8	5
EGR valve (% more open)	50	100	35
Throttle valve (% more open)	30	60	100

3. Sensitivity studies

The typical methodology followed to conduct mesh and time step sensitivity studies consists in first refining the mesh with a fixed time-step size until getting grid independence and then, with the final mesh, perform the time-step sensitivity [31, 4, 32]. However, both parameters are strongly related by the advective Courant number, presented in equation 1.

$$C = u \frac{\Delta t}{\Delta x} \tag{1}$$

In equation 1, u is the flow velocity, Δt is the time-step size and Δx is the size of the considered cell. This number quanti-

7

fies how many cells the advective information advances in every time step. When an explicit time-advancing scheme is employed, the so-called CFL condition requires $C \leq 1$ to assure the stability of the simulation [33]. For a compressible flow explicit solver, the wave speeds $|u \pm a|$ would play the role of the flow speed u in equation 1 [33], which further tightens the constraint. For transient implicit schemes relying on pressure corrections (such as the segregated solver used in this work), the theoretical limit is removed (the scheme is said to be unconditionally stable). However, in practical applications of implicit schemes with non-linear effects, the maximum Courant number allowed to avoid accuracy and stability issues may be about 1 for scale-resolving simulations [34] and close to 10 for URANS [35, 36] .

Considering equation 1, reducing the time-step size decreases the Courant number, so lower time-step sizes pose no problem. However, refining the mesh increases C, which could lead to the paradox of simulations with finer meshes but worse accuracy [37, 38].

In this work, the time-step size independence is addressed first. Apart from analyzing the sensitivity of time step on EGR distribution and subsequent pollutant emissions, the threshold of Courant number that creates issues will be assessed by studying the mass imbalance of the EGR species:

$$Imb[\%] = \frac{\int_{t_0}^{T} \sum \dot{m}_{EGR-outlet,i}(t)dt - \int_{t_0}^{T} \dot{m}_{EGR-inlet}(t)dt}{\int_{t_0}^{T} \dot{m}_{EGR-inlet}(t)dt} \cdot 100 \tag{2}$$

Starting from the baseline time-step size presented in section 2.2.3, a higher and two smaller time-step sizes have been calculated at working point 2, i.e., $\Delta t = 4°, 2°, 1°$ and $0.5°/step$. In this way, the presented cases will get significantly different Courant numbers (see equation 1), because the mesh is kept (6M cells) and flow velocities will be similar. The results of this study are presented in Figure 4 in terms of non-dimensional EGR deviations (Δy_{avg}, as defined in equation A.2).

Looking at Figure 4, most of the runners follow an asymptotic trend regarding the variable Δy_{avg} as time-step size is re-
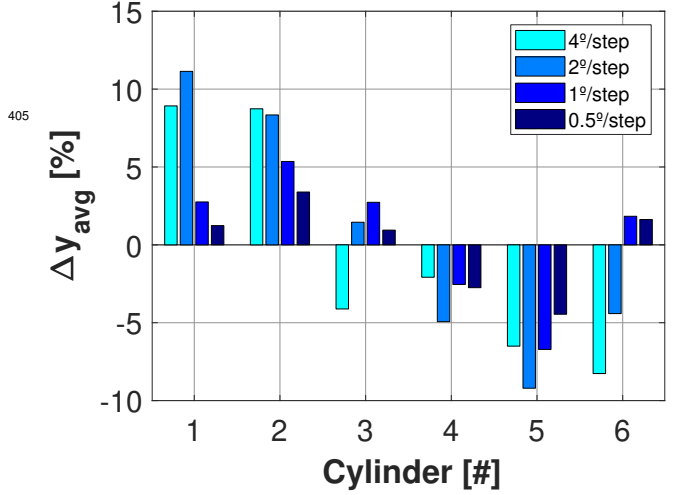

Figure 4: EGR rate deviation regarding Δy_{avg} for considered time-step sizes at working point 2.

duced, e.g., the closest case to the 0.5°/step is the 1°/step case. However, quantitative values are required to determine the point at which it is not worth it a further refinement of the time-step size. Therefore, the following paragraphs are devoted to the definition of coefficients to quantify the EGR cylinder-to-cylinder distribution and the related pollutant emissions.

A root mean square error ($RMSE$) index can be developed, to capture the differences in comparison with the reference case in terms of accuracy. For instance, for the time step sensitivity analysis, the reference case is 0.5°/step. After a normalization with the averaged EGR rate (equation 3), a global value for the considered cases is obtained. In addition, a coefficient of variance (COV) is defined in equation 4 to quantify the dispersion of a certain distribution of EGR rates. The higher the differences on EGR rate between each cylinder and the average, the greater will be the COV coefficient.

$$RMSE = \sqrt{\frac{\sum_{i=1}^{Z}(y_i - y_{i,ref})^2}{Z}} / \bar{y} \tag{3}$$

$$COV = \sqrt{\frac{\sum_{i=1}^{Z}(y_i - \bar{y})^2}{Z}} / \bar{y} \tag{4}$$

On the other hand, regarding the pollutant emissions, the developed models in section 2.1.2 will be useful to get an estimation of the differences between the analyzed cases. The λ

8

parameter will be considered constant for every cylinder, taking the value of the experimental essays corresponding to the working point assessed (in this section, operating point 2). Therefore, applying the regressions appearing in Figure 2, the pollutant emissions produced by each cylinder can be obtained as equations 5 and 6.

$$NOx_i/NOx_{EGR=0} = \frac{A \cdot e^{-B \cdot (y_i \cdot \lambda^{-1})}}{Z} \qquad (5)$$

$$FSN_i = \frac{A \cdot (y_i \cdot \lambda^{-1})^3 + B \cdot (y_i \cdot \lambda^{-1})^2 + C \cdot (y_i \cdot \lambda^{-1}) + D}{Z} \qquad (6)$$

Equations 5 and 6 assume that all cylinders present the same injection conditions and pressure in chamber. Hence, the impact of EGR dispersion predicted by a CFD simulation on emissions can be calculated using equations 5 and 6:

$$NOx \, [ppm] = \sum (NOx_i/NOx_{EGR=0}) \cdot NOx_{EGR=0} \qquad (7)$$

$$PM \, [g/h] = \frac{5.32 \cdot \sum (FSN_i) \cdot e^{0.3062 \cdot \sum (FSN_i)}}{0.405} \qquad (8)$$

The transformation from the filter smoke number (FSN) to the PM mass flow presented in equation 8 has been used previously in the work of Maiboom et al. [39]. The presented coefficients have been applied to the time step independence study as exposed in Table 2. In addition, an average of the Courant number (equation 1) in a section after the mixer and the mass flow rate imbalance (equation 2) are showed for all the cases.

Table 2: Coefficients of time-step size independence study at working point 2.

Coeff.	$RMSE$	COV	ΔNOx	ΔPM	$\overline{Cour}$	Imb.
Units.	[%]	[%]	[%]	[%]	[-]	[%]
4°/step	5.20	6.94	0.18	0.23	38.29	10.78
2°/step	4.79	7.31	0.20	0.26	18.28	5.17
1°/step	1.24	3.99	0.04	0.04	8.98	0.39
0.5°/step	-	2.71	-	-	5.10	0.35

Table 2 shows a significant improvement in terms of $RMSE$ when the time-step size is reduced from 2°/step to 1°/step, but
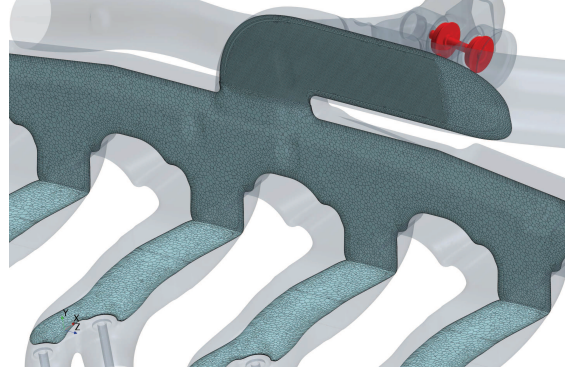

Figure 5: Sections of baseline mesh (6M cells) at manifold and cylinder runners.

seems not worth it to change the time-step size again to 0.5°/step due to the low changes. Regarding the pollutant emissions the changes are not so remarkable, and all the cases gets very similar results, so according to this criterion, the coarsest time-step size could be used. However, the changes in Courant are quasi-linear and the values in 4°/step and 2°/step are remarkable high, producing non negligible values of mass flow rate imbalance (above 5%). Discarding therefore the latter cases, the time-step size is fixed in 1°/step to the rest of the document to get a good trade-off between accuracy and computational effort.

When the time-step size is fixed, the mesh independence study can be addressed taking into account the aforementioned limitations of the Courant number. The baseline mesh of this work is presented in Figure 5. The highest density of elements is located in the mixer zone, to resolve the mixing between air and EGR streams in a proper way. Thereby, this zone will be critical in terms of Courant number, due to the high velocities coming from the air inlet and EGR valve, and the low cell size of the mesh. The relationship between the average cell size and the refinement size of the mesh is fixed for all the meshes. The baseline mesh presented in Figure 5 has 6M cells. 2 additional mesh have been developed to conduct the mesh independence study: a coarser mesh of 1.5M of cells and finer mesh of 15M elements. The results of the developed meshes in terms of Δy_{avg} (see equation A.2) are presented in Figure 6.

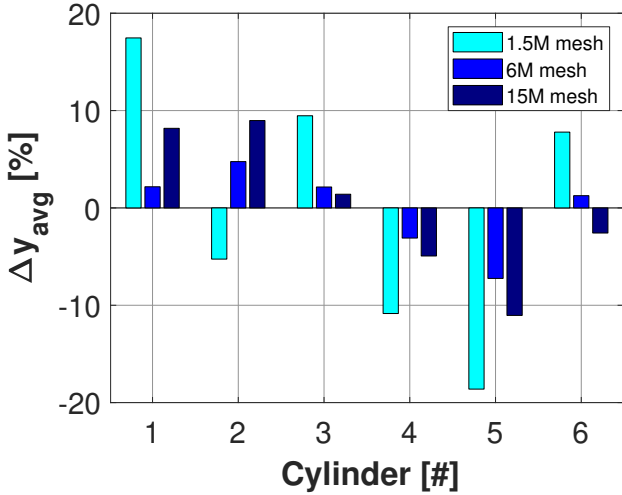As it can be noticed in Figure 6, some differences appear

9

Figure 6: EGR rate deviation regarding Δy_{avg} for different mesh refinements at working point 2.

between the 1.5M mesh and the higher refinement meshes of 6M and 15M. The coarsest mesh provides the greatest dispersion and, apparently, a higher error compared to the most accurate mesh of 15M celss This is confirmed in a quantitative way by considering the developed coefficients in equations 3, 4, 7, 8; which are obtained for this mesh independence study and presented in Table 3 with the corresponding values of mean Courant number and mass flow rate imbalance.

Table 3: Coefficients of mesh independence study at working point 2.

Coeff.	$RMSE$	COV	ΔNOx	ΔPM	$\overline{Cour}$	Imb.
Units.	[%]	[%]	[%]	[%]	[-]	[%]
1.5M	8.32	12.56	0.46	0.55	2.45	0.11
6M	3.30	3.99	-0.14	-0.18	8.98	0.39
15M	-	7.10	-	-	12.50	0.59

In terms of the $RMSE$ coefficient, the improvement by refining the mesh is significant when passing from a coarser mesh of 1.5M to a finer mesh of 6M, but this change is not so remarkable between the baseline mesh and the 15M mesh. Regarding the emissions indicators, the improvement in NOx and PM prediction as the mesh is refined is slight but consistent to the reduction of $RMSE$, with differences below 0.6%. The Courant number is obviously higher in the 15M mesh, but the

impact in terms of accuracy (imbalance) is negligible. Taking into account these coefficients, it seems a reasonable decision to maintain the 6M mesh as the final mesh for further validations. In any case, the coarser mesh of 1.5M could have been used with little penalty on emission predictions if computational resources were scarce.

4. Validation of turbulence models

Once the mesh and the time step size have been fixed, the numerical models must be validated against the experimental measurements. The structure of this section will be the same for every operating point: first, the average cylinder-to-cylinder EGR distribution is displayed, including a quantification of the differences between the predictions and the experimental measurements. Then, cycle-resolved traces of CO_2 are depicted and discussed.

It must be noticed that the numerical average results of this section are considered at the outlets of the domain (see Figure 3 and equation A.1) instead of employing the *Horiba* probes. By considering the real amount of EGR that enters into the cylinders, the comparison does not depend on flow heterogeneity inside the runners and is therefore consistent. Nevertheless, the average experimental results used in this section are extracted by the *Horiba* probes, so the deviations between CFD results obtained at *Horiba* probes and outlet boundaries are displayed in the experimental results, following the developed methodology in Appendix A.2 and applying the confidence intervals $(\mu \pm 2\sigma)$. On the other hand, the instantaneous results are extracted at the *Cambustion* probes, following the methodology of Appendix A.1.

4.1. Point 2

Since operating point 2 has been used in section 3 to perform the whole sensitivities studies, it will be the first point to assess in this validation process.

In Figure 7, the X-axis represents the cylinder of the engine while the Y-axis represents the EGR rate normalized with
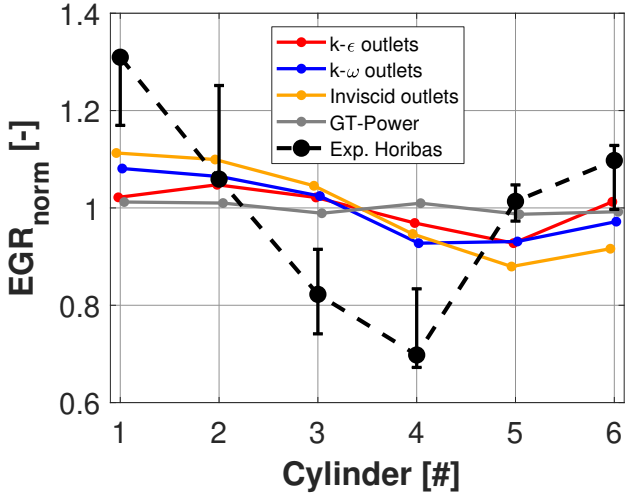
10

Figure 7: Normalized average of EGR rate at the outlets for the 3D-CFD models, 0D/1D model rates and experimental data at *Horiba* probes with experimental deviations of operating point 2.

the mean value, being considered at the outlets of the numerical models and the *Horiba* probes in the experimental data. As aforementioned, the experimental results are presented with vertical bars that indicate the trends of the real amount of EGR that the cylinder would swallow, taking into account the deviations in CFD of the *Horiba* probes (see Appendix A.2).

The comparison showed in Figure 7 shows how the 3D models provide similar patterns in terms of EGR rate dispersion, whereas the GT Power prediction without any 3D model is almost flat. In the experimental data, the EGR distribution has a pronounced "V" shape, with almost twice as much EGR rate in cylinder 1 than in cylinder 4. However, the deviation bars plotted in the experimental data suggest that the *Horiba* probes in this operating points may be overstating the EGR dispersion compared to what actually would be found in the cylinders.

To get a quantitative comparison, the coefficients used in section 3 have been applied in this validation section as well. The corresponding values of working point 2 are presented in Table 4. It must be noticed that the pollutants of the experiments used as reference in Table 4, are obtained by the regression developed in section 2.1.2 with the aim of applying the same methodology in all the EGR distributions. Apart from the

Table 4: Coefficients of Point 2 validation

Coeff.	$RMSE$	COV	ΔNOx	ΔPM
Units.	[%]	[%]	[%]	[%]
$k - \varepsilon$	16.23	3.99	-1.57	-1.83
$k - \omega$	14.51	6.06	-1.48	-1.72
Invis.	15.92	9.05	-1.29	-1.5
0D/1D	16.87	1.07	-1.63	-1.90
Uniform	17.02	0	-1.63	-1.91
Exp.	-	19.66	-	-

experimental measurements, the 3D CFD results and the engine model values, a uniform distribution is considered to see the impact of having a certain EGR dispersion in terms of emissions. In Table 4 the $RMSE$ of the EGR distributions are almost the same for every numerical model (even the 0D/1D model). The EGR dispersion (COV) is noticeable for the experimental measurements due to the "V" shape presented in Figure 7, lower for the 3D CFD simulations, and almost null for the 0D/1D model alone. These differences are translated into a $1.3\% - 2\%$ of error in prediction of NOx and PM emissions. As a summary, the numerical models fail to predict the V-shaped EGR distribution, even though the spatial sampling of the EGR dispersion could be responsible for a fraction of this difference.
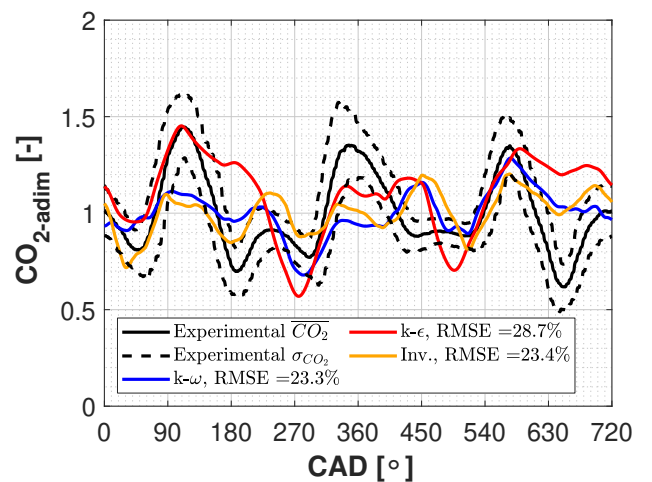

Figure 8: Normalized instantaneous traces of CO_2 for the 3D-CFD numerical models, and experimental data of operating point 2.

The cycle-resolved results are presented in Figure 8, in which

11

the X axis represents the crank angle degree of the engine while the Y axis represents the normalized (regarding the mean experimental percentage) instantaneous CO_2 percentage. In this plot, the cyclic dispersion of the experimental data is represented by a solid line (average values) and two dashed lines (upper and lower confidence intervales, considering one standard deviation σ).

Considering the instantaneous results plotted in Figure 8, the qualitative phasing of the experimental is captured in a reasonable way, but the amplitude of each event is not properly predicted. Quantitatively, the value of $RMSE$ is presented in Figure 8, being calculated regarding the mean line of the experimental trace.

4.2. Point 1

Operating point 1 was presented in Table 1 as a low load point with a medium-high EGR rate. This point is close to idle conditions. The comparison between time-averages EGR distributions is presented in Figure 9.
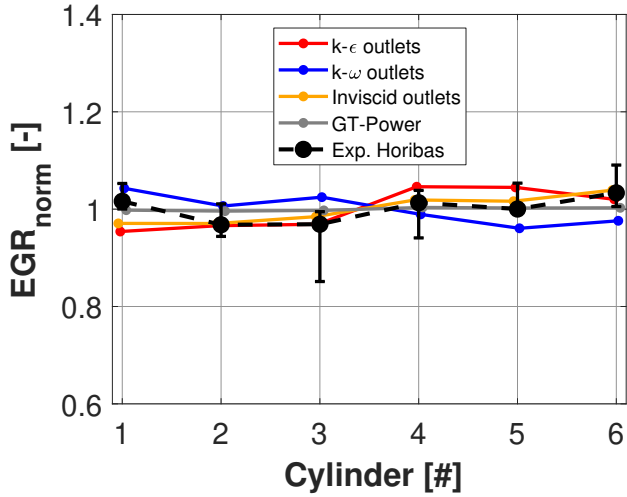

Figure 9: Normalized average of EGR rate at the outlets for the 3D-CFD models, 0D/1D model rates and experimental data at *Horiba* probes with experimental deviations of operating point 1.

The results depicted in Figure 9 shows that both experimental and numerical distributions are quite flat. Also, the vertical bars of the experimental deviations are much lower compared to the previous operating point (see Figure 7). This flat behavior in EGR distribution is common in operating points with low loads

and medium-high EGR rate as was demonstrated by William et al. [40].

Table 5: Coefficients of Point 1 validation

Coeff.	$RMSE$	COV	ΔNOx	ΔPM
Units.	[%]	[%]	[%]	[%]
$k-\varepsilon$	2.98	3.82	0.02	0.01
$k-\omega$	3.66	2.80	0.01	0.00
Invis.	1.82	2.61	0.00	0.00
0D/1D	1.93	0.29	-0.02	0.00
Uniform	2.10	0	-0.02	0.00
Exp.	-	2.43	-	-

Observing the numerical coefficients presented in Table 5 for this operating point, the $RMSE$ of the 3D models is almost the same, while the 0D/1D is even closer to the experimental results. Due to the flat behavior presented in Figure 9, the differences in terms of pollutant emissions are negligible.
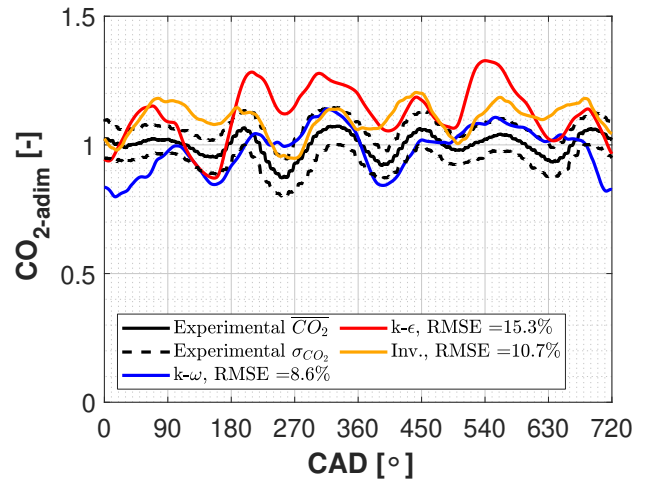

Figure 10: Normalized instantaneous traces of CO_2 for the 3D-CFD numerical models, and experimental data of operating point 1.

Regarding the instantaneous comparisons presented in Figure 10, the $SST\ k-\omega$ submodel is closer to the experimental trace than the other numerical models, presenting a good qualitative and quantitative prediction of the experimental small fluctuations of CO_2. The oscillations of $k-\varepsilon$ submodel are much more aggressive, despite the smoothing effect due to the running average process explained in Appendix A.1.

12

4.3. Point 3

Operating point 3 was presented before in Table 1 as the point with greatest power, employing a low EGR rate. The average results of this operating point in terms of EGR cylinder-to-cylinder distribution are presented in Figure 11.
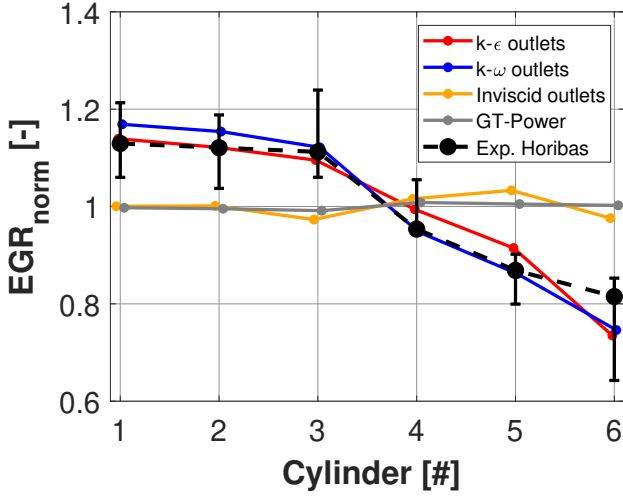

Figure 11: Normalized average of EGR rate at the outlets for the 3D-CFD models, 0D/1D model rates and experimental data at *Horiba* probes with experimental deviations of operating point 3.

The patterns of the EGR dispersion shown in Figure 11 for operating point 3 are the only ones that strongly depend on the considered numerical model. The 0D/1D model is clearly not able to reproduce the experimental results, providing a flat distribution in the same way than the other operating points (Figure 7 and Figure 9). The inviscid approach presents poor average results too, with a very flat distribution, almost the same than the 0D/1D model. On the contrary, both $k-\varepsilon$ and SST $k-\omega$ are clearly able to reproduce the behavior of the experimental results, in which there is a monotonous decrease in EGR rate when increasing the cylinder number. In fact, both submodels are within the intervals defined by the *Horiba* deviation bars.

As expected, the coefficients in Table 6 show the clear agreement between $k-\varepsilon$ and SST $k-\omega$ submodels and the experimental results, in terms of low $RMSE$ and similar COV. Nevertheless, in terms of pollutant emissions the differences between approaches (even uniform distribution) are very low, showing little sensitivity of emissions to EGR dispersion at this operat-

Table 6: Coefficients of Point 3 validation

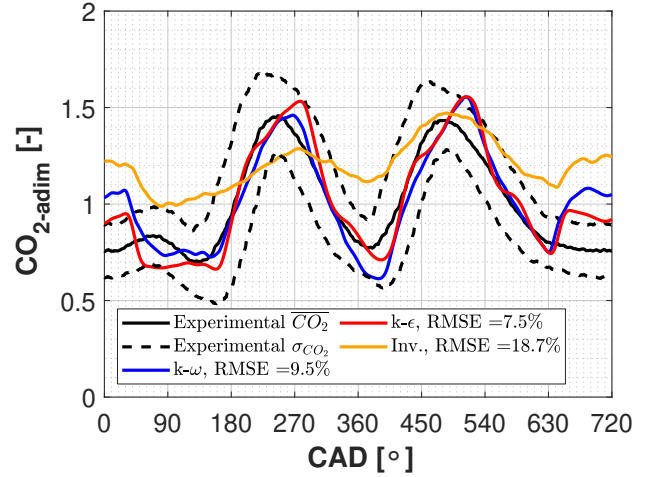| Coeff.	$RMSE$	COV	ΔNOx	ΔPM
Units.	[%]	[%]	[%]	[%]
$k-\varepsilon$	3.63	14.19	0.02	-0.03
$k-\omega$	3.07	15.98	0.21	-0.20
Invis.	11.57	2.10	-0.27	0.30
0D/1D	11.42	0.58	-0.28	0.31
Uniform	11.04	0	-0.28	0.31
Exp.	-	12.75	-	-

ing point.

Figure 12: Normalized instantaneous traces of CO_2 for the 3D-CFD numerical models, and experimental data of operating point 3.

The instantaneous comparison presented in Figure 12 is in accordance with the average results because both $k-\varepsilon$ and SST $k-\omega$ present a remarkable agreement with the experimental trace of CO_2. On the other hand, the inviscid model is not able to predict the phasing and intensity of the oscillations in a proper way.

4.4. Sensitivity of emissions to EGR dispersion

For all the cases analyzed in this section, the error in terms of pollutant emissions (NOx and PM) against the experimental results are below 2%. Since even uniform distributions have been considering, with $RMSE$ reaching values of 17% (see Table 4), the impact of EGR distribution on emissions is low for

13

the studied working points. In the remaining part of this section, a quantitative interpolation is conducted in order to assess the sensitivity of emissions to EGR dispersion at different operating conditions, considering a EGR flat distribution as a baseline. To do so, two degrees of freedom are considered. On the one hand, $EGR \cdot 1/\lambda$ factor presented in Figure 2, which carries the information of the engine working point. On the other hand, the dispersion itself, which takes into account the mixer and manifold design. To be able to change the latter, the original difference between the EGR rate on a certain cylinder and the average EGR rate is modified by a factor k, thus keeping the same mean EGR. Therefore, the modified EGR rate in the cylinder will be calculated as:

$$EGR_{i-mod} = y_{i-mod} = (y_i - \overline{y}) \cdot k + \overline{y}, \qquad k \geq 0. \qquad (9)$$

Notice that $k = 0$ in equation 9 provides a flat distribution whereas $k = 1$ is the original EGR cylinder-to-cylinder dispersion. In this way, the regressions shown in equations 5 and 6 allow to interpolate the NOx and PM pollutant emissions of the 6 cylinders by means of modifying the average EGR (and thus $EGR \cdot 1/\lambda$) or dispersion proportionality factor k in equation 9.

These emissions are normalized considering the contaminants that a flat distribution with the same mean level of $EGR \cdot 1/\lambda$ factor, would produce, i.e.,

$$\varepsilon_{NOx}(k) \; [\%] = \frac{NOx(k) - NOx(k = 0)}{NOx(k = 0)} \cdot 100 \qquad (10)$$

$$\varepsilon_{PM}(k) \; [\%] = \frac{PM(k) - PM(k = 0)}{PM(k = 0)} \cdot 100 \qquad (11)$$

This analysis is only conducted for working point 2, due to its high dispersion as was presented in Figure 7. The evolution of ε_{NOx} and ε_{PM} in terms of $EGR \cdot 1/\lambda$ and k is presented in Figure 13:

The situation studied in this work for working point 2 ($EGR \cdot 1/\lambda = 8$, as shown in Table 1, and $k = 1$) is represented as a dot in Figure 13, with a difference in emissions between the actual case and a flat distribution below 2% (see Table 4). Considering the same dispersion proportionality factor $k = 1$, an increase in
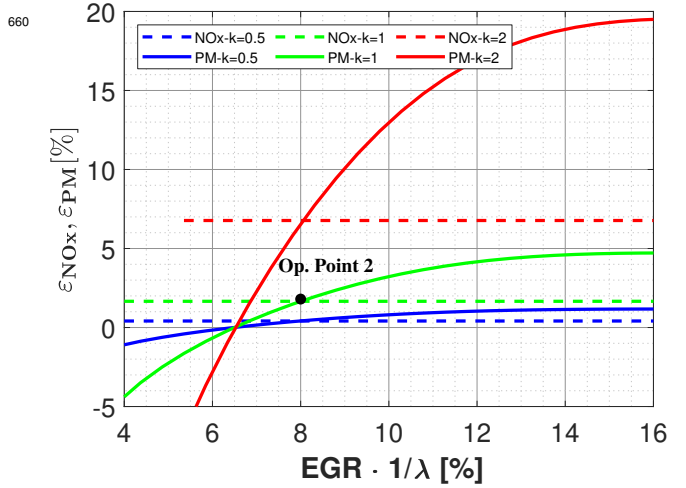

Figure 13: Relative differences of NOx and PM emissions between dispersed and flat EGR distributions for Operating Point 2.

EGR rates to fulfil future emission standards does not affect to the importance of EGR distribution in NOx (green dashed line), due to its exponential regression law (Figure 2). On the contrary, the PM fitting suggests an increasing importance of EGR dispersion as the EGR rate is higher, reaching an asymptotic behavior of 5% when doubling the EGR rate ($EGR \cdot 1/\lambda = 16$) with the current dispersion ($k = 1$).

If the dispersion was reduced (blue lines in Figure 13 correspond to $k = 0.5$), the impact of EGR dispersion in emissions would be 1% at worst-case scenario. In this way, the effort of predicting the cylinder-to-cylinder EGR distribution is likely not justified. However, if the manifold or mixer design provide a strong EGR dispersion (red lines in Figure 13 correspond to $k = 2$), an accurate prediction of the EGR distribution is mandatory. For operating point 2 with current EGR rate, NOx emissions would be miscalculated by 7% if EGR dispersion is neglected. This error would reach 13% for PM (red solid line) with a future situation in which EGR rate is increase by 25% ($EGR \cdot 1/\lambda = 10$). Macián et al. [15] also noticed a sudden rise in PM emissions at highest $EGR \cdot 1/\lambda$ when EGR dispersion is increased.

14

5. Analysis of numerical flow field

In section 4, the average and instantaneous results of the numerical models have been compared with the experimental results. In this section, the flow field is analyzed so as to provide some insight on the underlying reasons of the differences between operating points and turbulence models found in section 4.

5.1. Sensitivity to turbulence model

Figure 11 showed that, for operating point 3 (high power), the inviscid model predicts a very flat distribution of EGR, especially in comparison with the $SST\ k-\omega$ submodel. Figure 14 presents the time-averaged EGR mass fraction in 2 postprocessing lines, placed at the inlet of the manifold and across the middle of the manifold body, respectively (these lines are plotted in Figure 3). The traces are plotted from right to the left (regarding Figure 3) and with a normalized length. The spatial distribution predicted by the inviscid case in Figure 14 is very similar to EGR dispersion plotted in Figure 11: Y_{EGR} has a very flat behavior, at the inlet and middle of the manifold (Figure 14) as well as the runner outlets (Figure 11). On the contrary, the $SST\ k-\omega$ submodel presents a significant dispersion at Figure 11, promoting greater EGR mass fractions at cylinders 1-2-3 than at cylinders 4-5-6. This is translated into a similar pattern in terms of EGR dispersion (Figure 11), even though the differences between EGR rates and the average value have been diluted as the cylinders breath in from the manifold.

To confirm the trends that Figure 14 has showed, the contours of time-averaged Y_{EGR} and velocity vectors for operating point 3 in both cases ($SST\ k-\omega$ and inviscid) are represented in Figure 15.

In the inviscid case (upper part of Figure 15), there is a significant mixing between the air and EGR streams before reaching the manifold. On top of that, the elbow turns the flow almost 90°, creating vortices on the meam flow that further promote the mixing, providing a uniform EGR rate across the manifold. These flow features of the inviscid case are in agreement to the flat EGR distributions shown in Figures 11 and 14.
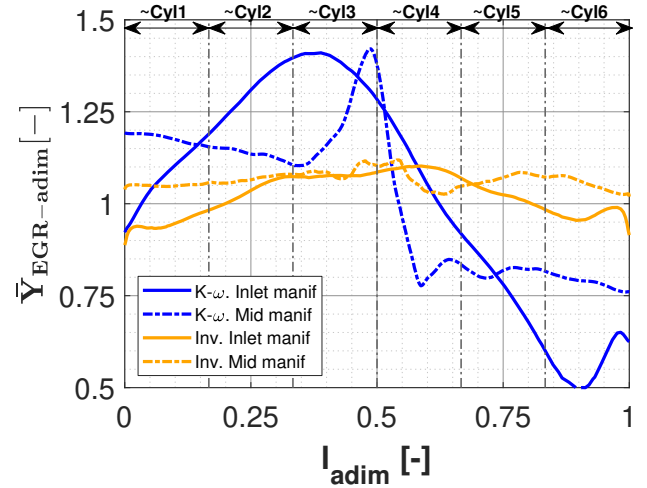

Figure 14: Mean Y_{EGR} on postprocessing lines, of $SST\ k-\omega$ submodel and inviscid approach at operating point 3.

Regarding the $SST\ k-\omega$ turbulence submodel (lower part of Figure 15), the stream of fresh air is only slightly deflected by the elbow, being therefore oriented to the left branch of the manifold (where cylinders 4-5-6 are, in accordance with Figure 3). This motion induces a detachment of the flow at the middle of the manifold, creating a low-pressure vortex that aspirates the mass of EGR located at the upper part of the inlet duct. This EGR stream surrounds the fresh air jet and then is redirected to the manifold right side (corresponding to cylinders 1-2-3). This behavior of the $SST\ k-\omega$ predicted flow explains the EGR dispersion pattern appearing in Figures 11 and 14.

5.2. Shift of operating point

Once different turbulence submodels have been compared with the same boundary conditions (working point 3), it could be interesting to compare different operating points considering the turbulence submodel, to understand the differences in the EGR distribution shown in Figures 7 and 9. Figure 16 depicts the same variables and planes than Figure 15 in operating points 1 and 2 with the $SST\ k-\omega$ turbulence submodel in both cases.

The time-averaged velocity in the manifold calculated with $SST\ k-\omega$ for operating points 1, 2 (Figure 16) and 3 Figure 15 is similar: the flow from the main duct is directed mainly to the left side of the manifold creating a small vortex in the upper part of this side. However, the U-turn required for the
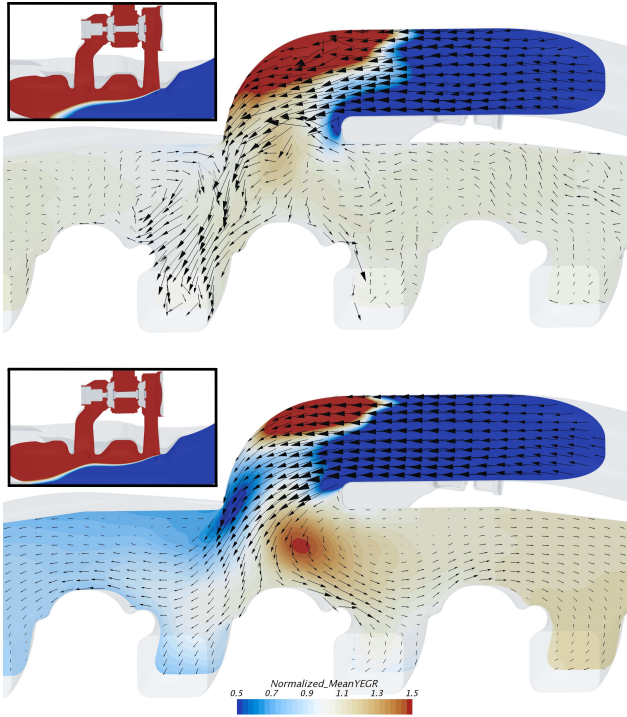
15

Figure 15: Mean Y_{EGR} contours with mean velocity vectors on mid plane of the manifold and sketch of mean Y_{EGR} on mixer plane of inviscid model (top) and $SST \ k - \omega$ submodel (bottom) at operating point 3.

Figure 16: Mean Y_{EGR} contours with mean velocity vectors on mid plane of the manifold and sketch of mean Y_{EGR} on mixer plane of $SST \ k - \omega$ submodel at operating point 1 (top) and 2 (bottom).

flow in the main duct to achieve the right part of the manifold is not possible in operating point 3 (lower part of Figure 15) due to its greater momentum (highest engine speed as shown in table 1), while this path is feasible for working point 1 (upper part of Figure 16) in accordance to its lower momentum (lowest engine speed). For operating point 2 (lower part of Figure 16), only a small fraction of flow coming from the main duct is able to reach directly the right side of the manifold.

Besides, the behavior of the flow next to the mixer (close ups at Figures 15 and 16) differs between operating points 2 and 3, in which the EGR flow is attached to the upper side of the main duct (more extreme for point 3) and working point 1 (top of Figure 16). For the latter, the higher EGR rate (see table 1)) allows the exhaust gases to penetrate deeper into the air stream, promoting a greater mixing before even reaching the manifold and causing a flat EGR distribution.

The comparison of flow fields also explains why point 2 is more challenging to be predicted, as confirmed by the disagreement between numeri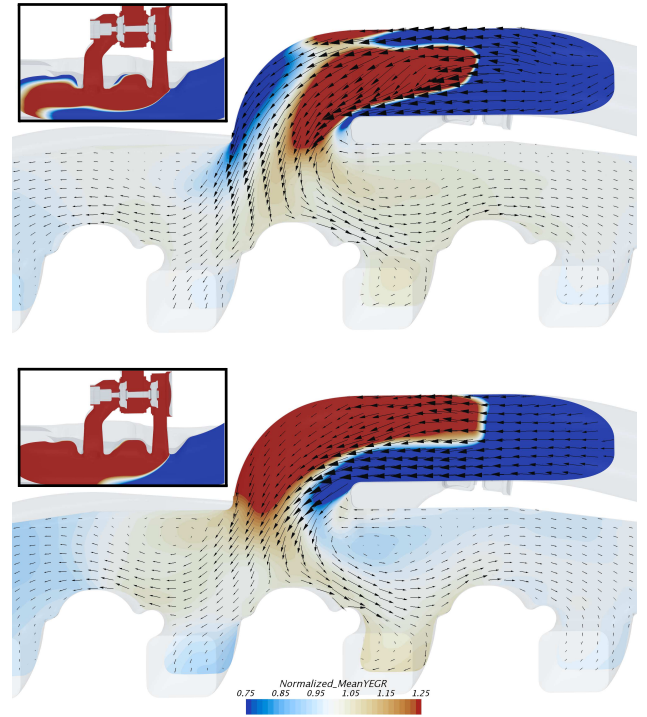cal and experimental results depicted in Figure 7. Since the flow is between two different modes in terms of air and EGR mixing in the main duct as well as ability for the flow of the main duct to turn 180°to the left side of the manifold, the flow field could more sensitive to small changes, such as the one produced by the uncertainties of the model. Besides, the local heterogeneity of mean Y_{EGR} shown in bottom side of Figure 16 explain why the *Horiba* probes can depart significantly from the actual EGR rate that would get into the cylinders, as represented by the large vertical bars of Figure 7

6. Concluding remarks

From this study, the following conclusions can be extracted:

- The methodology to predict EGR cylinder-to-cylinder distribution based on experiments, engine modeling and 3D CFD simulations of the inlet manifold has been analyzed.

- Experimental probes for measuring average CO_2 can present significant deviations (up to 20%) when assessing the

EGR swallowed by each cylinder, regardless of being located in the corresponding runner.

- A statistical regression for NOx and PM emissions is obtained, allowing to quantify the impact of EGR dispersion on emissions.

- When conducting mesh and time-step independence analysis, the Courant number must be considered, despite using transient implicit schemes. In this work, average advective Courant numbers above 15 result in lack of EGR mass conservation (imbalances greater than 5%).

- At low power conditions, EGR distribution is flat, which is properly predicted even by the 0D/1D engine code alone (without CFD 3D). CO_2 transient traces present small oscillations and are qualitatively well captured even by the inviscid model. The homogeneity of the flow is explained by the good mixing between the EGR and air in the main duct, which sends the flow evenly to both sides of the manifold.

- The working point at medium power presents a "V-shaped" EGR distribution with significant dispersion, even though its impact on NOx and PM emissions is below 2% compared to a flat distribution. The statistical regression suggests a greater sensitivity of emissions to EGR dispersion (7% for NOx and 13% for PM) if the EGR rate is increased by 25% and the dispersion is doubled. The proposed methodology (engine model+CFD 3D) fails at predicting the EGR distribution in terms of average EGR dispersion ($RMSE \approx 15$) and CO_2 transient traces ($RMSE \approx 15$). The flow behavior is challenging, as the mixer works in an intermediate mode and only a small fraction of the main duct flow is able to turn into the right side of the manifold. The flow presents significant concentration gradients, which cause the greatest deviations between the local CO_2 probes and their corresponding cross-section value (which contributes to the predicting error). Scale-resolving simulations such as LES [19, 27] could there-

fore present greater accuracy than URANS at these conditions.

- At high power conditions, EGR distribution is monotonously decreasing, which is properly predicted only by $k - \varepsilon$ and $k - \omega$ turbulent submodels. CO_2 transient traces present significant oscillations which are accurately captured by these models, whereas the inviscid configuration provides a much flatter response. Flow field investigation reveals that a detachment of the flow coming from the main duct into the manifold explains the EGR asymmetry, which is not predicted by the inviscid model.

List of Symbols

a	speed of sound	$m \cdot s^{-1}$
C	Courant number	–
$\epsilon_{outlets}$	error *Horiba*-outlet	-
λ	excess of air factor	-
Imb	EGR mass imbalance	%
N	engine speed	*rpm*
u	velocity magnitude	$m \cdot s^{-1}$
n	number of cycles	-
y	EGR rate	-
Z	Number of cylinders	-

Sub- and Superscripts

adim	non-dimensional
i	runner
norm	normalized
ref	reference value

17

List of abbreviations and acronyms

0D	zero dimensional
1D	one dimensional
3D	three dimensional
BMEP	brake mean effective pressure
CFD	computational fluid dynamics
COV	coefficient of variance
CO_2	Carbon dioxide
EGR	exhaust gas recirculation
FSN	filter smoke number
HP-EGR	high pressure EGR
ICE	internal combustion engine
LES	large eddy simulation
LP-EGR	low pressure EGR
M	millions of cells
NOx	Mono-Nitrogen oxides
Op	operating point
RANS	Reynolds-averaged Navier-Stokes
RMSE	Root mean square error
rpm	revolutions per minute
URF	under-relaxation factor

References

[1] N. Ladommatos, S. Abdelhalim, H. Zhao, The effects of exhaust gas recirculation on diesel combustion and emissions, International Journal of Engine Research 1 (1) (2000) 107–126 (2000). doi:10.1243/1468087001545290.

[2] J. M. Desantes, J. M. Luján, B. Pla, J. A. Soler, On the combination of high-pressure and low-pressure exhaust gas recirculation loops for improved fuel economy and reduced emissions in high-speed direct-injection engines, International Journal of Engine Research 14 (1) (2013) 3–11 (2013). doi:10.1177/1468087412437623.

[3] J. M. Luján, C. Guardiola, B. Pla, A. Reig, Switching strategy between HP (high pressure)-and LPEGR (low pressure exhaust gas recirculation) systems for reduced fuel consumption and emissions, Energy 90 (2015) 1790–1798 (2015). doi:10.1016/j.energy.2015.06.138.

[4] J. Galindo, P. Piqueras, R. Navarro, D. Tarí, C. Meano, Validation and sensitivity analysis of an in-flow water condensation model for 3D-CFD simulations of humid air streams mixing, International Journal of Thermal Sciences 136 (2019) 410 – 419 (2019). doi:10.1016/j.ijthermalsci.2018.10.043.

[5] J. Serrano, P. Piqueras, R. Navarro, D. Tarí, C. Meano, Development and verification of an in-flow water condensation model for 3D-CFD simulations of humid air streams mixing, Computers & Fluids 167 (2018) 158 – 165 (2018). doi:10.1016/j.compfluid.2018.02.032.

[6] J. Galindo, R. Navarro, D. Tarí, G. García-Olivas, Centrifugal compressor influence on condensation due to Long Route-Exhaust Gas Recirculation mixing, Applied Thermal Engineering 144 (2018) 901 – 909 (2018). doi:10.1016/j.applthermaleng.2018.09.005.

[7] S. Karstadt, J. Werner, S. Münz, R. Aymanns, Effect of water droplets caused by low pressure EGR on spinning compressor wheels, in: Aufladetechnische Konferenz, Dresden, 2014 (2014).

[8] F. Millo, P. F. Giacominetto, M. G. Bernardi, Analysis of different exhaust gas recirculation architectures for passenger car diesel engines, Applied energy 98 (2012) 79–91 (2012). doi:10.1016/j.apenergy.2012.02.081.

[9] J. M. Luján, J. Galindo, J. R. Serrano, B. Pla, A methodology to identify the intake charge cylinder-to-cylinder distribution in turbocharged direct injection diesel engines, Measurement Science and Technology 19 (6) (2008) 065401 (2008). doi:10.1088/0957-0233/19/6/065401.

[10] A. Maiboom, X. Tauzia, J.-F. Hétet, Influence of egr unequal distribution from cylinder to cylinder on nox–pm trade-off of a hsdi automotive diesel engine, Applied Thermal Engineering 29 (10) (2009) 2043 – 2050 (2009). doi:10.1016/j.applthermaleng.2008.10.017.

[11] J. M. Luján, H. Climent, B. Pla, M. E. Rivas-Perea, N.-Y. François, J. Borges-Alejo, Z. Soukeur, Exhaust gas recirculation dispersion analysis using in-cylinder pressure measurements in automotive diesel engines, Applied Thermal Engineering 89 (2015) 459–468 (2015). doi:10.1016/j.applthermaleng.2015.06.029.

[12] CD-adapco, STAR-CCM+, release version 12.06.010 Edition (February 2018).
URL http://ww.cd-adapco.com

[13] C. Guardiola, B. Pla, D. Blanco-Rodriguez, P. O. Calendini, ECU-oriented models for NOx prediction. Part 1: a mean value engine model for NOx prediction, Proceedings of the Institution of Mechanical Engineers, Part D: Journal of Automobile Engineering 229 (8) (2015) 992–1015 (2015). doi:10.1177/0954407014550191.

[14] X. Tauzia, H. Karaky, A. Maiboom, Evaluation of a semi-physical model to predict nox and soot emissions of a ci automotive engine under warm-up like conditions, Applied Thermal Engineering 137 (2018) 521–531 (2018). doi:10.1016/j.applthermaleng.2018.04.005.

[15] V. Macián, J. M. Luján, H. Climent, J. Miguel-García, S. Guilain, R. Boubennec, Cylinder-to-cylinder high-pressure exhaust gas recirculation dispersion effect on opacity and no x emissions in a diesel automotive engine, International Journal of Engine Research (2020) 1468087419895401 (2020). doi:10.1177/1468087419895401.

[16] R. Rahimi, S. Jafarmadar, S. Khalilarya, A. Mohebbi, Numerical and experimental investigations of EGR distribution in a DI turbocharged diesel engine, Transactions of the Canadian society for mechanical engineering

37 (2) (2013) 247–257 (2013). doi:10.1139/tcsme-2013-0015.

[17] S. Ramanathan, A. Hudson, J. Styron, B. Baldwin, D. Ives, D. Ducu, EGR and swirl distribution analysis using coupled 1D-3D CFD simulation for a turbocharged heavy duty diesel engine, Tech. rep., SAE Technical Paper (2011). doi:10.4271/2011-01-2222.

[18] S. K. R. Hariganesh, M. Sathyanadan, S. Krishnan, P. Vadivel, D. Vamsidhar, Computational analysis of EGR mixing inside the intake system & experimental investigation on diesel engine for LCV, International Journal of Engineering Science & Technology 3 (3) (2011).

[19] A. Sakowitz, L. Fuchs, Computation of mixing processes related to EGR, in: TSFP digital library online, Begel House Inc., 2011 (2011).
URL http://www.dl.begellhouse.com/en/references/3ce1b491115b5c16,60d8a9681cb3cfc7,57130c5b30e27450.html

[20] A. Sakowitz, M. Mihaescu, L. Fuchs, Turbulent flow mechanisms in mixing T-junctions by Large Eddy Simulations, International Journal of Heat and Fluid Flow 45 (2014) 135–146 (2014). doi:10.1016/j.ijheatfluidflow.2013.06.014.

[21] M. Georgiou, M. V. Papalexandris, Turbulent mixing in T-junctions: The role of the temperature as an active scalar, International Journal of Heat and Mass Transfer 115 (2017) 793–809 (2017). doi:10.1016/j.ijheatmasstransfer.2017.08.081.

[22] A. Sakowitz, Computation and analysis of egr mixing in internal combustion engine manifolds, Ph.D. thesis, KTH Royal Institute of Technology (2013).
URL http://www.diva-portal.org/smash/record.jsf?pid=diva2:603864&dswid=6780

[23] S. Reifarth, E. Kristensson, J. Borggren, A. Sakowitz, H.-E. Angstrom, Analysis of EGR/Air Mixing by 1-D Simulation, 3-D Simulation and Experiments, Tech. rep., SAE Technical Paper (2014). doi:10.4271/2014-01-2647.

[24] P. Dimitriou, R. Burke, C. D. Copeland, S. Akehurst, Study on the effects of EGR supply configuration on cylinder-to-cylinder dispersion and engine performance using 1D-3D co-simulation, Tech. rep., SAE Technical Paper (2015).
URL https://saemobilus.sae.org/content/2015-32-0816

[25] V. J. Page, C. P. Garner, G. K. Hargrave, H. K. Versteeg, Development of a validated CFD process for the analysis of inlet manifold flows with EGR, Tech. rep., SAE Technical Paper (2002). doi:10.4271/2002-01-0071.

[26] P. Dimitriou, C. Avola, R. Burke, C. Copeland, N. Turner, A Comparison of 1D-3D Co-Simulation and Transient 3D Simulation for EGR Distribution Studies, in: ASME 2016 Internal Combustion Engine Division Fall Technical Conference, American Society of Mechanical Engineers, 2016, pp. V001T06A010–V001T06A010 (2016). doi:10.1115/icef2016-9361.

[27] A. Sakowitz, S. Reifarth, M. Mihaescu, L. Fuchs, Modeling of EGR Mixing in an engine intake manifold using LES, Oil & Gas Science

and Technology–Revue dIFP Energies nouvelles 69 (1) (2014) 167–176 (2014). doi:10.2516/ogst/2013118.

[28] J. Galindo, H. Climent, R. Navarro, G. García-Olivas, S. Guilain, R. Boubennec, Effect of Numerical Configuration on Predicted EGR Cylinder-to-Cylinder Dispersion, Tech. rep., SAE Technical Paper (2020). doi:10.4271/2020-01-1113.

[29] B. Pla, Análisis del proceso de la recirculación de los gases de escape de baja presión en motores diesel sobrealimentados, Ph.D. thesis, PhD Thesis, Universitat Politècnica de València, Departamento de Máquinas y Motores Térmicos (2009). doi:10.4995/Thesis/10251/4782.

[30] Galindo, José and Climent, Héctor and Navarro, Roberto, Modeling of EGR Systems, in: A. Onorati, G. Montenegro (Eds.), 1D and Multi-D Modeling Techniques for IC Engine Simulation, SAE International, 2020, Ch. 7, pp. 257–278 (2020). doi:10.4271/9780768099522.

[31] R. Navarro, Predicting Flow-Induced Acoustics at Near-Stall Conditions in an Automotive Turbocharger Compressor: A Numerical Approach, Springer, 2018 (2018). doi:10.1007/978-3-319-72248-1.

[32] Sharma, Sidharath and García-Tíscar, Jorge and Allport, JM and Barrans, Simon and Nickson, AK, Evaluation of modelling parameters for computing flow-induced noise in a small high-speed centrifugal compressor, Aerospace Science and Technology 98 (2020) 105697 (2020). doi:10.1016/j.ast.2020.105697.

[33] Ferziger, J.H. and Perić, M., Computational Methods for Fluid Dynamics, 3rd Edition, Springer, 2002 (2002).

[34] R. M. Cummings, S. A. Morton, D. R. McDaniel, Experiences in accurately predicting time-dependent flows, Progress in Aerospace Sciences 44 (4) (2008) 241–257 (May 2008). doi:10.1016/j.paerosci.2008.01.001.

[35] B. Lakshminarayana, An Assessment of Computational Fluid Dynamic Techniques in the Analysis and Design of TurbomachineryThe 1990 Freeman Scholar Lecture, Journal of Fluids Engineering 113 (3) (1991) 315–352 (09 1991). arXiv:https://asmedigitalcollection.asme.org/fluidsengineering/article-pdf/113/3/315/5592525/315_1.pdf, doi:10.1115/1.2909503.

[36] F. Balduzzi, A. Bianchini, R. Maleci, G. Ferrara, L. Ferrari, Critical issues in the cfd simulation of darrieus wind turbines, Renewable Energy 85 (2016) 419 – 435 (2016). doi:10.1016/j.renene.2015.06.048.

[37] S. Družeta, L. Sopta, S. Maćešić, N. Črnjarić-Žic, Investigation of the importance of spatial resolution for two-dimensional shallow-water model accuracy, Journal of Hydraulic Engineering 135 (11) (2009) 917–925 (2009). doi:10.1061/(asce)0733-9429(2009)135:11(917).

[38] Z. Boz, F. Erdogdu, M. Tutar, Effects of mesh refinement, time step size and numerical scheme on the computational modeling of temperature evolution during natural-convection heating, Journal of Food Engineering 123 (2014) 8–16 (2014). doi:10.1016/j.jfoodeng.2013.09.008.

[39] A. Maiboom, X. Tauzia, J.-F. Hetet, Influence of high rates of supplemental cooled EGR on NOx and PM emissions of an automotive HSDI diesel engine using an LP EGR loop, International Journal of Energy Research

32 (15) (2008) 1383–1398 (2008). `doi:10.1002/er.1455`.

[40] J. William, A. Dupont, R. Bazile, M. Marchal, Study of geometrical parameter influence on air/EGR mixing, SAE transactions (2003) 1016–1036 (2003). `doi:10.4271/2003-01-1796`.

Appendix A.

Appendix A.1. Virtual probes postprocessing

Taking into account the virtual probes presented in Figure 3 it is necessary a brief description of how the EGR rate is obtained depending of the considered probe or analysis. In section 2.2.3, it was exposed that the EGR is modeled itself as one species of the simulation (the other is the air species). Therefore, the EGR rate in the outlets of the domain (see Figure 3) can be defined as:

$$EGR_i = y_i = \frac{m_{EGR} \ [kg]}{m_{tot} \ [kg]} \approx \frac{\sum_{j=1}^{720} \left(\dot{m}_{EGR-j} \cdot \Delta t \right)}{\sum_{j=1}^{720} \left(\dot{m}_{tot-j} \cdot \Delta t \right)} \quad (A.1)$$

Where i indicates every cylinder of the manifold, $\dot{m}_j$ is the EGR or total mass flow through the outlet of the domain, and Δt is the time-step size. Thereby, the amount of EGR or total mass of flow swallowed by the cylinders is calculated. To get non-dimensional values, these rates can be presented as deviations against the mean EGR of the case as presented in equation A.2

$$\Delta y_{avg} = \frac{y_i - \bar{y}}{\bar{y}} \quad (A.2)$$

where $\bar{y}$ is the mean EGR rate of the 6 cylinders. This deviation of equation A.2 regarding the average value is used in the sensitivity studies of section 3. In addition, as explained in section 2.1, the *Horiba* probes have been used to measure the mean EGR rate of a certain cylinder. These probes are placed in the manifold in the most representative zones of the cylinders (see Figure 3), taking into account the restrictions of space in the experimental facility. Thus, the rate in these virtual sensor are useful to obtain the deviations between *Horiba* and outlet of Appendix A.2. Considering the *Horiba* probes, the EGR rate can be defined as:

$$EGR \approx \frac{m_{EGR} \ [kg]}{m_{tot} - m_{HORIBA} \ [kg]} \quad (A.3)$$

If the *Horiba* probes are used to get the EGR rate, and considering the mass flow rate extracted by the *Horiba* as constant:

$$EGR_{HORIBA}(t) \approx \frac{\dot{m}_{\widehat{HORIBA}} \cdot Y_{EGR}(t) \cdot \cancel{\Delta t}}{(\dot{m}_{\widehat{HORIBA}} \cdot Y_{air}(t) + \dot{m}_{\widehat{HORIBA}} \cdot Y_{EGR}(t)) \cdot \cancel{\Delta t}} \quad (A.4)$$

Therefore, the EGR rate in the numerical *Horiba* probes can be approximated using only the mass fraction of EGR ($Y_{EGR}(t)$), due to the EGR is modeled as an species of the simulation. This mass fraction can be obtained by a mass flow average [12]:

$$Y_{EGR}(t) = \frac{\sum_f \rho_f Y_{EGR-f} |\mathbf{v}_f \cdot \mathbf{a}_f|}{\sum_f \rho_f |\mathbf{v}_f \cdot \mathbf{a}_f|} \quad (A.5)$$

In equation A.5, ρ_f is the density of a certain face of the surface, and $\mathbf{v}_f$ and $\mathbf{a}_f$ are the velocity and area vectors respectively. Hence, the final EGR rate in a certain *Horiba* probe can be obtained as:

$$Y_{EGR-i} = \frac{\sum_1^n \sum_{CAD} Y_{EGR}(t)/CAD}{n}, \quad n = 1, 2...cycles \quad (A.6)$$

Regarding the instantaneous results, it is necessary to develop a specific method to make proper comparisons between numerical results and experimental data. The *Cambustion* sensor of the CFD domain has been presented in Figure 3. In terms of CO_2 percentage, the EGR rate can be defined according to Luján et al. [9] as:

$$EGR \ [\%] = \frac{[CO_2]_{intake} - [CO_2]_{atm}}{[CO_2]_{exhaust} - [CO_2]_{atm}} \cdot 100 \quad (A.7)$$

Taking into account that $[CO_2]_{atm} \sim 0$, the CO_2 percentage of the CFD calculations can be obtained as:

$$[CO_2]_{intake-CFD} \ [-] = EGR_{Camb}[\%] \cdot \frac{\rho}{\rho_{EGR}} \cdot [CO_2]_{exhaust}, \quad (A.8)$$

being EGR_{Camb} the mass fraction of EGR of the virtual probe and $[CO_2]_{exhaust}$ the percentage of CO_2 in the exhaust for the considered operating point (as measured in essays). Finally, the experimental instantaneous results will present an inherent averaging or *smoothing* effect due to the huge amount of measured cycles and the finite time that the probe needs to analyze the flow composition at each sample. In order to apply this effect to the CFD traces, a moving average is employed using *Matlab* © . This function performs an average on a certain element of an array considering a number of adjacent elements. The size of the window k_{avg} in which the average is performed, will depend of the sensor sampling period T_{sensor}, and the time step of the numerical simulation Δt_{CFD}, as presented in equation A.9. This *smoothing* correction is applied to all the instantaneous numerical traces of section 4.

$$k_{avg} \ [-] = \frac{T_{sensor}}{\Delta t_{CFD}} \tag{A.9}$$

Appendix A.2. Experimental deviations

It must be noticed that the measured EGR rate by the *Horiba* probes (in a experimental and numerical way, obtained in equation A.6) may not be the same than the real EGR that the cylinder swallows (the EGR in the outlets, see Figure 3 and equation A.1). Thus, the impact of performing the experimental measurements in the *Horiba* probes instead of in the intake ports must be assessed. The experimental data in these ports is not available, but an approximation of these deviations can be obtained by means of the CFD calculations. First, the numerical deviation between *Horibas* (local surface) and outlets (whole cross-section) can be calculated:

$$\varepsilon_{outlet-i} = Y_{Horiba-i} - Y_{outlet-i} \tag{A.10}$$

Therefore, for every outlet of the domain the corresponding $\varepsilon_{outlet-i}$ can be obtained. To perform a reliable statistical analysis, it is convenient to consider a large number of cases for every operating point. In this way, additional cases that are not directly analyzed in this work have been used for this particular

study to increase the population of the statistical analysis. Consequently, for every $\varepsilon_{outlet-i}$ (normalized with the average EGR rate) and operating point, an average (μ) and standard deviation (σ) are extracted after adjusting the population to a normal distribution. An average p-value of 0.04 is obtained considering all the fittings conducted for the different cylinders and operating points. The distributions of $\varepsilon_{outlet-i}$ for operating point 2 are presented in Figure A.17:
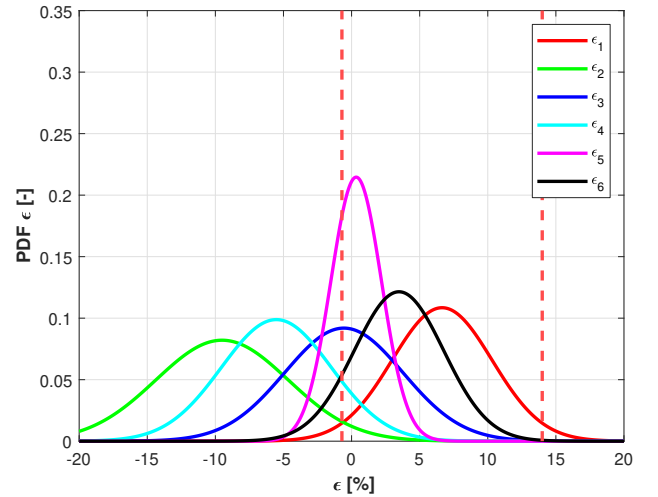

Figure A.17: Adjusted normal probability distribution functions for $\varepsilon_{outlet-i}$ in operating point 2. The dashed vertical bars correspond to the 95% criterion ($\mu \pm 2\sigma$) for $\varepsilon_{outlet-1}$.

In Figure A.17, in cylinder 5 the deviation between taking the measurement in the *Horiba* probe instead in the outlet is small and does not present bias. However, in other cylinders the mean of the deviations is noticeable (up to 10%) with important standard deviations. Therefore, the error of taking the measurement in the *Horiba* probes will depend of the considered cylinder and operating point and it is remarkable in some cases. With this statistical fitting of the deviations calculated with CFD, an assessment of the uncertainty of the experimental measurements due to this fact is showed in Figures 7, 9 and 11 as vertical bars.